Disruption halo current rotation scaling on Alcator C-Mod and HBT-EP

A.R. Saperstein,[1] R.A. Tinguely,[2] R.S. Granetz,[2] J.P Levesque,[1] M.E. Mauel,[1] and G.A. Navratil[1]
[1)]*Department of Applied Physics and Applied Mathematics, Columbia University, New York, NY 10027, United States of America*
[2)]*MIT Plasma Science and Fusion Center, Cambridge, MA 02139, United States of America*

(*Electronic mail: alex.saperstein@columbia.edu)

(Dated: 3 March 2023)

Asymmetric halo currents (HCs) can exert large net forces on the vacuum vessel and other components during disruptions on tokamaks. The displacements caused by these forces can then be amplified if these asymmetric forces rotate at frequencies resonant with the vessel. This paper reports on the investigation of a recently proposed scaling law for the disruption HC rotation frequency[1] that combines measurements on Alcator C-Mod with those on HBT-EP. We find that a new non-circular version of the scaling law ($\frac{<f_{rot}>}{m/<m>} \propto \frac{1}{B_T(S/\pi)}$) takes into consideration the dependence of f_{rot} on the poloidal structure of the MHD instability (m) driving the asymmetry and describes the disruption-averaged rotation frequency on C-Mod. Disruption rotation is also found to be insensitive to the vertical position and impurity content of the plasma at the onset of the disruption.However, a stagnation in the time-evolution of f_{rot} is occasionally observed. Observations are consistent with the dominance of poloidal rotation during the disruption, which is motivated by the poloidal drift nature of the scaling law.

I. INTRODUCTION

Disruption events on tokamaks release large amounts of stored magnetic energy that can potentially damage the vacuum vessel and other components. This damage is mediated through electro-magnetic loads, which are associated with the currents driven in the walls. Asymmetries in these currents can lead to the most dangerous of these loads, and the displacements associated with these asymmetries can be amplified when their rotation matches the resonant frequencies of the walls and/or other components. This motivates a better understanding of the rotation of the asymmetries in these wall-currents, so that resonances might be avoided and lessen the severity of the electro-magnetic loads.

Currents can be transferred to the walls either inductively via the current quench (CQ) as eddy currents, or via direct contact between the plasma and the wall as halo currents (HCs). Both current sources are susceptible to asymmetries and resonances; however, this paper reports on the measurements of HC rotation, so they are focused on here.

The mechanisms responsible for HC asymmetries (and subsequently their rotation) are still an open topic of research[2–6]; however, a connection to the rotation of MHD instabilities has been recognized since the 90's[7,8] and experimental observations correlating the two have been observed previously[9–12]. These studies suggest that the rotation of the HC asymmetries is tied to that of MHD instabilities with low toroidal mode numbers. This connection has also been observed in the simulation of disruptions with 3D codes, where low-order kink modes were found to introduce slowly rotating toroidal asymmetries in the plasma current[15].

The first scaling law for the asymmetric HC rotation frequency empirical matched experimental observations on large high-field tokamaks[13]. But this scaling law under-predicted the rotation on HBT-EP[12], a smaller low-field tokamak, by more than an order of magnitude[1]. A new physically motivated scaling law was then introduced[1], consistent with rotation governed by a poloidal drift. This scaling for the rotation frequency of the asymmetric halo currents during the CQ was described by

$$f_{rot} = \frac{A}{B_T a^2} \tag{1}$$

where B_T is the on-axis toroidal magnetic field strength, a is the minor radius of the plasma, and A is a constant that varies weakly with other machine parameters (and is $292\,[HzTm^2]$ based on a multi-machine fit). Like the previous empirical scaling law, this scaling law was accurate over a database of machines spanning various sizes and field strengths. However, the new scaling law improves upon the previous scaling by simultaneously describing the rotation on HBT-EP, which exists at an extremum of these scaling parameters, allowing the scaling law to be accurate over three orders of magnitude in rotation frequencies. In addition, this new scaling was found to be capable of predicting the dynamic evolution of the HC rotation frequency throughout disruptions on the HBT-EP tokamak.

In this paper, the new scaling law is further investigated by combining HBT-EP measurements with the halo current rotation observations on Alcator C-Mod[14]. The investigation on C-Mod takes advantage of an equivalent version of the scaling law that includes shaping effects

$$f_{rot} = \frac{A}{B_T(S/\pi)} \tag{2}$$

where S is the poloidal cross-sectional area of the plasma, and the factor of π was added to be consistent with the scaling law in equation (1). We find that despite the large difference in parameters between C-Mod and HBT-EP, their disruption rotation and HC physics share many similarities. However, C-Mod gives evidence of other influences to the HC rotation. These include (i) the dependence on q_{edge} (through its relationship to the poloidal structure of the mode driving the rotating asymmetry), and (ii) the stagnation of the evolution of the rotation frequency even as the plasma cross-sectional area changes throughout the disruption. Finally, the C-Mod observations show that the scaling law is insensitive to the vertical

position and impurity content of the plasma at the onset of the disruption.

The remainder of this paper is organized into the following sections. Section II discusses how disruptions on C-Mod are characterized, as well as the general characteristics of their rotating halo current asymmetries (RHCAs), and compares them to the observations on HBT-EP. Section III looks at the average disruption rotation on C-Mod in the context of the scaling law, and then adds a correction to the scaling law related to the edge safety factor to account for the poloidal structure of the MHD instabilities driving the RHCAs. Section IV investigates the insensitivity of the rotation characteristics to the vertical position and impurity content of the plasma at the onset of the disruption. Section V compares the different parameterizations of the scaling law used for the multi-machine scaling and the individual machine scalings of HBT-EP and C-Mod. Section VI provides evidence consistent with the dominance of poloidal rotation during the disruption. And finally, section VII concludes the paper.

II. THE CHARACTERIZATION OF C-MOD DISRUPTIONS

This section will discuss the measurements and characterizations of disruptions and RHCAs on Alcator C-Mod, a compact ($R \sim 68cm$, $a \sim 22cm$) high-field ($B_T \sim 5.4T$) conventional tokamak, operated with moderate plasma current ($I_p \sim 1MA$) and edge safety factor ($q_{95} \sim 5 \rightarrow 6$), and with both shaped and diverted plasmas. These characteristics are then compared to those on HBT-EP[1], a low-field limited tokamak. The first subsection will discuss how these disruption parameters are measured, and the second will then discuss the observations in detail.

A. Disruption measurements on C-Mod

The relevant global plasma parameters were measured using a filament-based equilibrium reconstruction code, which was developed at MIT for the express purpose of characterizing disruptions on C-Mod. This reconstruction produced the plasma cross-sectional area (S), vertical position (Z_p), and edge safety factor (q_{edge}). An example output of this reconstruction is shown in Figure 1. q_{95} was used as the relevant q_{edge} for characterizing edge MHD instabilities. The uncertainty in q_{95} associated with the lack of internal measurements was small, given that q_{95} agreed with q_{LCFS} to within 2% during the limited periods of the disruptions.

C-Mod's plasmas were elongated throughout the their disruptions ($1 < \kappa < 1.8$), so the non-circular version of the scaling law given in equation (2) was used. The substitution of a^2 with S was appropriate given that the poloidal drift motivation for the scaling assumes a^2 corresponds to the cross-sectional area of a circular plasma. The factor of π was included here to consistently map a^2 to S.

The diagnostics used to measure halo currents on C-Mod were a toroidal array of partial Rogowski coils, the locations

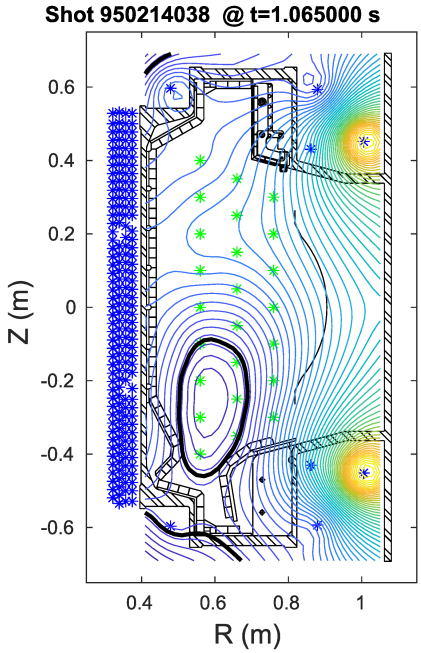

FIG. 1: Sample filament equilibrium reconstruction output for the disruption of shot 950214038 on C-Mod. The blue stars are coil positions, the green stars are the fixed plasma filament locations, and the resulting ψ_p contours are plotted over the machine geometry with the LCFS as a thicker line.

of which are shown in Figure 2 and are described in detail in Granetz *et al*[8]. These partial Rogowski coils measured the poloidal component of the HCs passing between the inboard (HFS) and outboard (LFS) sides of the divertor, and are capable of tracking the rotation of the asymmetric HCs throughout the duration of the disruption.

The rotation frequency (f_{rot}) of the asymmetric HCs on C-Mod was averaged over for each disruption. This was done because few complete rotations were observed for any given disruption on C-Mod, allowing the significant errors associated with the onset and termination of rotation to make up a significant portion of the total rotating period. $<f_{rot}>$ was calculated manually for each of the 69 disruptions included in the frequency analysis. This avoided the underestimation of $<f_{rot}>$ often observed when automating the analysis for cases with fewer than two complete rotations. The manual analysis consisted of both (i) tracking the times between peaks on a single sensor to get a period ($<f_{rot}>=\frac{1}{n}\Sigma\tau_n^{-1}$) if two or more complete rotations were made and (ii) tracking peaks as they move toroidally across sensors to get a phase difference over time ($<f_{rot}>=\Delta\theta/2\pi\tau$) if fewer than two complete rotations were made.

A single plasma cross-section was chosen to accompany each measurement of $<f_{rot}>$. The relevant cross-section selected corresponded to the time where an asymmetric peak is first noticeable in the HC sensor array (as indicated by the dashed purple line shown later in Figure 4(b)). This was chosen because a stagnation in the evolution of f_{rot} was observed

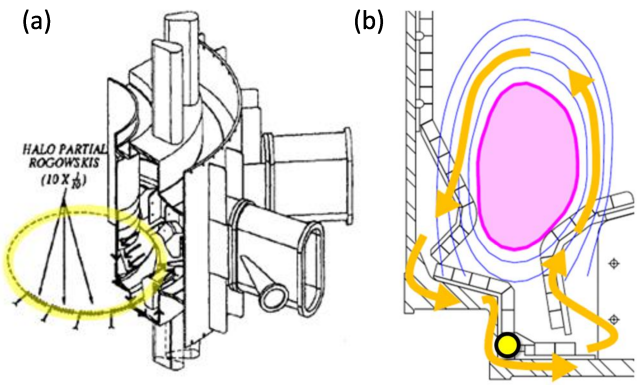

FIG. 2: Locations of the partial Rogowskis used to measure halo currents. (a) View of the toroidal array highlighted in yellow, with 10 sensors in total. Reproduced courtesy of IAEA. Figure from Granetz *et al*[8]. Copyright 1996 IAEA. (b) Poloidal cross-section of the lower-divertor, with a sample reconstruction illustrating contact between the plasma and the wall. The yellow dot shows the location of the partial Rogowskis.

following the onset of many of the RHCAs on C-Mod, implying other effects were playing a more significant role at those times. The choice of S at the onset of the RHCA would then minimize the significance of this effect.

B. Disruption and halo current characteristics on C-Mod

Disruptions on C-Mod share many of the same characteristics as those on other devices including HBT-EP, some of which are illustrated in Figure 3. The disruptions have two stages, first a thermal quench ($\tau_{TQ} \sim 100\mu s$) and then a current quench ($\tau_{CQ} \sim 2ms$). The duration of the TQ is consistent with the plasma's L/R-time assuming a post-CQ temperature similar to that on most other devices ($O(10eV)$). The plasma moves vertically towards one of it's divertors (often the lower one) and the plasma shrinks in size as it transitions from being diverted to limited. The shrinking of the plasma cross-section often occurs faster than the current quenches, resulting in q_{95} decreasing. As the current quenches, large HCs are driven in the walls, becoming as large as 25% of the total pre-disruption plasma current. The symmetric component of these currents correlates very well with dI_p/dt (as shown in Figure 4(b)), which is consistent with the inductive current drive in the scrape-off layer region.

The decrease in q_{95} can then lead to the destabilization of MHD instabilities that drive asymmetries in the HCs, like that seen in Figure 4(b). The HC asymmetries can be as large in magnitude as their symmetric counterparts. However, not every disruption that has q_{95} drop to low values sees the growth of a rotating mode, which suggests a sensitivity to some other stability parameters of the plasma that have not yet been identified. The toroidal array of HC sensors typically indicate an $n = 1$ structure for these asymmetries, and they make anywhere between $<1 \rightarrow 7$ complete rotations, with most cases completing fewer than two complete rotations. Of the cases where at least one complete rotation is made, the rotation frequency is observed to range between $1 \rightarrow 8$ kHz. Toroidal rotation is always in the counter-I_p direction, even when the direction of I_p is reversed (which appears as a flip in the direction of rotation in the lab-frame). The rotation frequency also often does not change significantly as the disruption evolves, and in some cases slows down like that shown in Figure 4(b).

The main differences observed between disruptions on C-Mod and HBT-EP are the duration and dynamics of the RHCAs. On HBT-EP, a rotating asymmetry is observed throughout the entire disruption, while on C-Mod it takes some time to appear. This may be because C-Mod operates at a higher pre-disruption q_{95} than HBT-EP ($q_{95}(C\text{-}Mod) \sim 5 \rightarrow 6$ vs $q_{95}(HBT\text{-}EP) \sim 3$), which makes it take longer for q_{95} to decrease to an unstable value like 2 (see the q_{95} profile in Figure 3). This is corroborated with the observation that rotating asymmetries become destabilized around $q_{95} \sim 2$ on C-Mod (shown later in Figure 6). This rotation onset time is therefore not necessarily universal, and depends on both q_{95} at the onset of the disruption and the rate at which q_{95} decreases.

The fact that the evolution of the rotation frequency on C-Mod stagnates and does not increase in time as the plasma cross-section shrinks, like it does on HBT-EP, is the most significant difference. It suggests other effect(s) are acting on the HC rotation rate, for example the cooling of the plasma is one potential mechanism. Future work should investigate the time-evolution of the HC rotation and determine if this is effect is expected to be significant on other tokamaks.

III. HALO CURRENT ROTATION SCALING ON C-MOD

This section investigates the validity of the scaling law given in equation (2) on C-Mod, measured using the methods described in section IIA. The investigation reveals a dependence on the poloidal MHD mode structure (as indicated by the edge safety factor). The first subsection examines the scaling law given in equation (2) and demonstrates that the C-Mod machine-averaged rotation is consistent with it. The second subsection introduces a modified version of the scaling law that includes a dependence on q_{onset} (q_{95} at the onset of the RHCA) through the poloidal mode structure that drives the asymmetry. This modified version of the scaling is shown to recover the linearity between $<f_{rot}>$ and the scale-factor that is missing in the un-modified analysis on C-Mod.

A. Investigating the scaling law without an edge q modification

The average rotation frequencies and corresponding scale factors ($1/B_T(S/\pi)$), specified in equation (2), are plotted for C-Mod in Figure 5 as the blue dots. For comparison, we have also included a projection of the linear fit of the HBT-EP database (reported in Saperstein *et al*[1]) extrapolating to the region of $1/B_T(S/\pi)$-space for the C-Mod data. From this

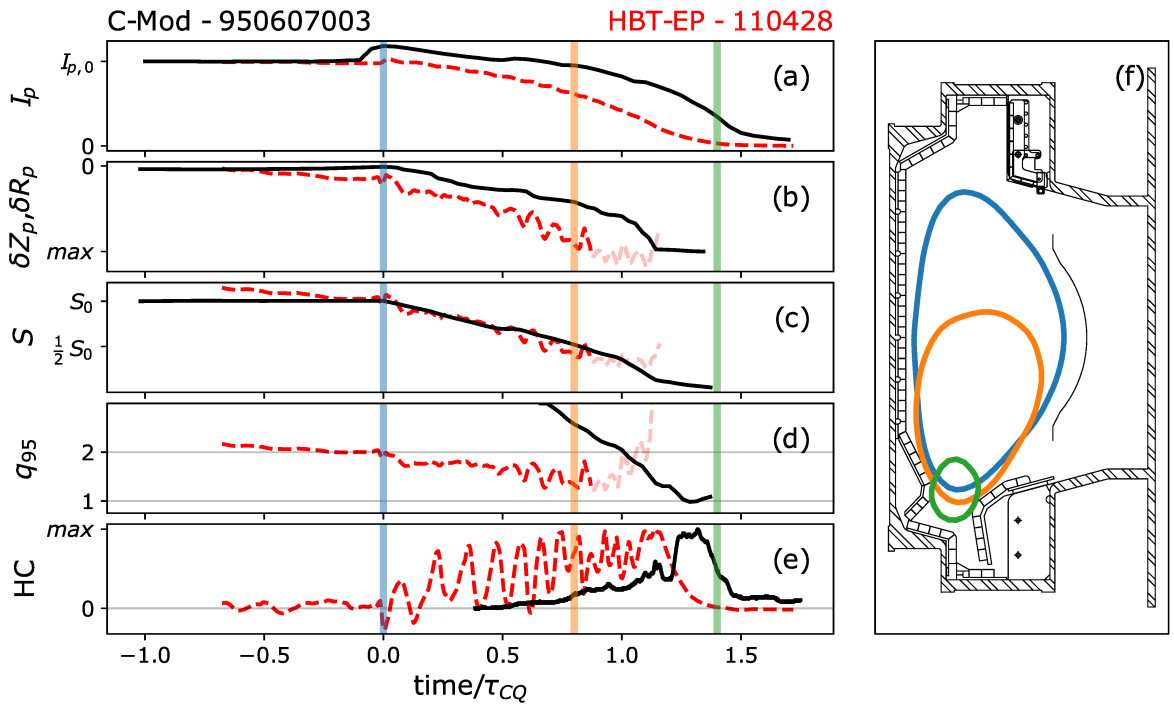

FIG. 3: Disruption characteristics on C-Mod and HBT-EP. Disruption curves of (a) I_p, (b) centroid position (Z_p for C-Mod and R_p for HBT-EP), (c) cross-section area, (d) q_{95}, and (e) sample HC signals. C-Mod curves are in black while HBT-EP profiles are in red (and dashed). Signal units are normalized for comparison between machines except in the case of q_{95}, and time-axis is normalized to the current quench time (defined separately for the two disruptions). (f) LCFS of the C-Mod plasma at the three times shown in the temporal profiles, denoted by the vertical lines with corresponding colors.

comparison, it is clear that the overall rotation observed on C-Mod is consistent with the HBT-EP scaling. The C-Mod scatter about this prediction is larger than that seen in the HBT-EP database, but the difference doesn't exceed more than a factor of 5.

The main difference between the HBT-EP scaling and the C-Mod scaling shown in Figure 5 is that the C-Mod data do not show a clear linear trend between $<f_{rot}>$ and $1/B_T(S/\pi)$ when viewed in isolation like HBT-EP does. This linearity is recovered, however, when the poloidal structure of the MHD instability driving the RHCA is included in the scaling law. This is discussed in the next subsection.

B. Investigating the scaling law with an edge q modification

In the development of the scaling law, a couple of parameters were absorbed into the scaling pre-factor (A in Saperstein *et al*[1]) because they were not expected to change significantly from machine-to-machine. One of these parameters is the poloidal structure of the MHD instability driving the RHCA (m). The inclusion of m comes from the conversion of a poloidal velocity to an apparent poloidal rotation frequency when some periodicity is present ($f_{rot} = \frac{m}{2\pi a} u_\theta$), and it is not expected to change significantly from machine-to-machine because m is expected to be of order unity ($m \sim O(1)$) for all machines. However, while this effect may not be significant when making comparisons over large scales, it is possible that a noticeable effect could become significant when examining disruptions in the context of a single machine. This subsection will show that this effect is not only significant on C-Mod, but that it also explains the lack of a linear relationship between $<f_{rot}>$ and $1/B_T(S/\pi)$ in Figure 5. Section III B 1 describes how the q_{95} measured at the onset of each RHCA (q_{onset}) is translated to the poloidal mode structure (m) for each case. Section III B 2 explicitly demonstrates the significance of this dependence by comparing the rotation observed for two cases where the scale-factors ($1/B_T(S/\pi)$) are the same but there is a difference in q_{onset}. And finally, section III B 3 introduces the modified version of the scaling that recovers the linearity between the rotation frequency and scale-factor on C-Mod.

1. *Identifying m using q_{onset}*

In order to determine if differences in m are having a significant effect, it is first necessary to be able to characterize m for the asymmetries in a given disruption. During the disruption, the plasma moves far from most of the magnetic sensors, making them inadequate for use in identifying m. This leaves q_{onset} as the best indicator of the poloidal structure of the mode.

Simulations of NSTX[15] and observations of m and q_{onset} in JET[11] and HBT-EP disruptions suggest that the MHD instabil-

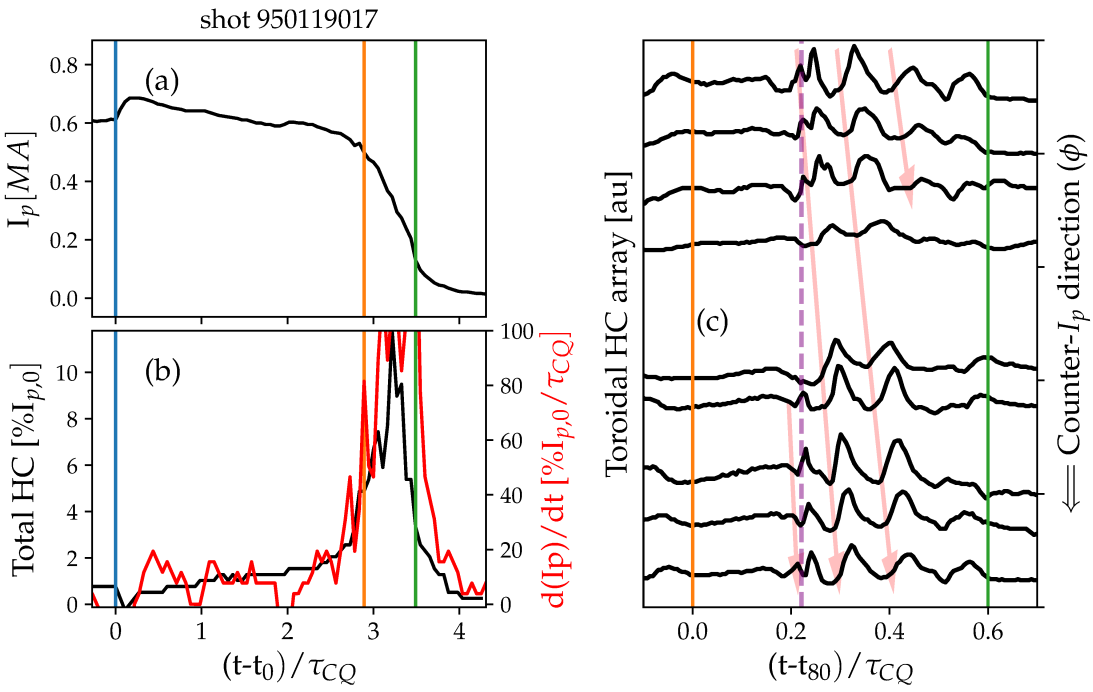

FIG. 4: Halo current characteristics on C-Mod for shot 950119017. Disruption curves of (a) I_p, (b-black) total poloidal HC normalized to pre-disruption plasma current, $I_{p,0}$, and (b-red) dI_p/dt normalized to $I_{p,0}$ and the CQ time for that disruption, τ_{CQ}. The time-axis is shifted to start at the current-spike and is normalized τ_{CQ}. (c) HC signals for 9 of the 10 toroidal partial Rogowski sensors stacked vertically in order of their toroidal positions. Red arrows were drawn on top to follow the growth/rotation of the asymmetry and the vertical dashed purple line is the location in time of the first peak. The time-axis is shifted to start when I_p reaches 80% its pre-disruption value (vertical orange line) and is also normalized to τ_{CQ}.

ities driving the RHCAs are external kink modes, which implies that q_{onset} can be a good indicator of m if n is also known. Ideal kink stability states that the most unstable mode for a given n will have a poloidal structure described by $m = nq_{ext}$, where q_{ext} is the lowest integer value of q outside the LCFS. For $n = 1$ (observed as the dominant toroidal structure in the HC measurements on C-Mod), this approximately maps q_{onset} to m through $m = ceiling(q_{onset}) = \lceil q_{onset} \rceil$, which is used to determine m for the following analyses. The error associated with possibly misclassifying an $m = 2$ mode as an $m = 3$ mode for values of q_{onset} close to but just above 2 is minimal, considering that there are relatively few cases of q_{onset} at these values (see Figure 6).

The distribution of q_{onset} for each disruption case examined on C-Mod is shown in Figure 6. We see that q_{onset} always remains above 1 and below 3, implying that the poloidal mode numbers are either $m = 2$ or $m = 3$. This is similar to what is seen for HBT-EP[1], which also has $q_{95} > 1$ throughout its CQs, but differs from the JET observations[11] which see a mode grow after q_{95} falls below 1, resulting in an $m = 1$ magnetic structure instead.

2. *Comparing two disruptions with different* q_{onset}

The effect of m on $<f_{rot}>$ is exemplified by comparing two separate disruptions where the only significant parameter that changes between the two is their m-number. Two such disruptions are shown in Figure 7. Both disruptions are caused by vertical displacement events (VDEs), triggered by the excess injection of lithium, have similar CQ times (suggesting similar temperatures), the same B_T, and similar plasma cross-sections at the onset of their RHCAs. The latter two similarities suggest that the unmodified scaling law would predict the same rotation frequency. The main difference between the two disruptions is that I_p is smaller in one case, resulting in a larger q_{95} throughout the disruption and a larger q_{onset}. Based on $m = \lceil q_{onset} \rceil$, the m-number associated with the high-q_{95} case is 3 and that of the low-q_{95} case is 2.

Figure 8(a) plots the HC signals for the two cases with the times shifted such that $t = 0$ is roughly the onset-time of the RHCA. Tracking the motion of the peaks between the two cases shows that the high-q_{95} case rotates faster. The difference in frequencies ($\sim$ 1.8 kHz vs $\sim$ 2.5 kHz) is consistent with the expected factor of $\sim$ 1.5x associated with the difference between a dominant $m = 2$ and $m = 3$ periodicity. This is shown in Figure 8(b) by scaling the time-base of the high-q_{95} disruption by a factor of 1.5, which results in the overlapping

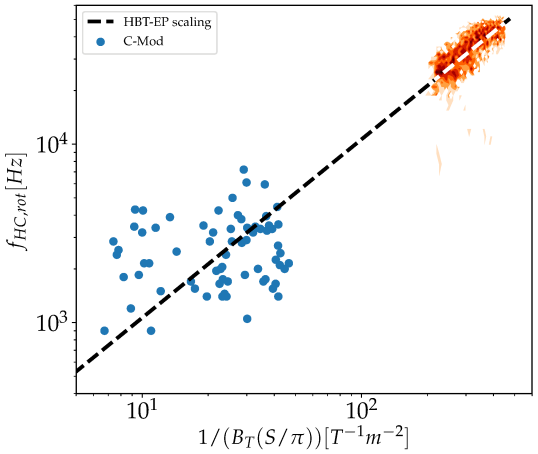

FIG. 5: HC rotation frequencies plotted against $1/B_T(S/\pi)$ for both the disruption-averaged C-Mod data (blue dots) and the dynamic HBT-EP data (red histogram). The dashed black line is the linear fit of the HBT-EP data, and is projected down in $1/B_T(S/\pi)$ to where the C-Mod data exist.

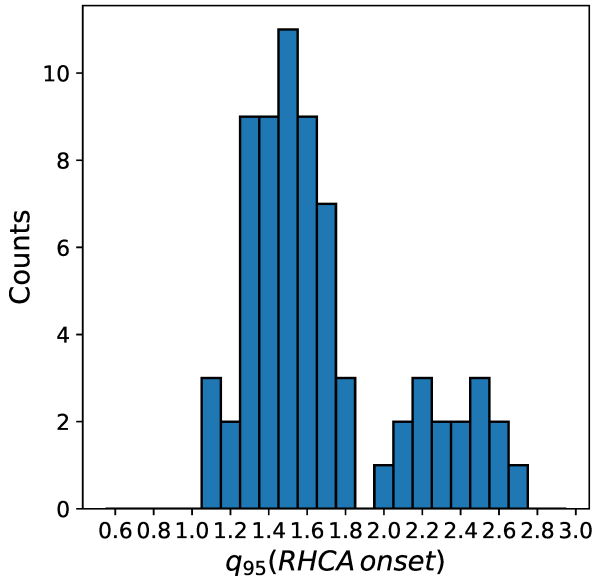

FIG. 6: Distribution of q_{onset} on C-Mod.

of the peaks in both cases.

3. *Improvement due to the modified scaling law*

We can now take into consideration the effect of the poloidal mode number by modifying the scaling law to normalize $<f_{rot}>$ to the m-number.

$$\frac{<f_{rot}>}{m/<m>} = A^* \frac{1}{B_T(S/\pi)} \tag{3}$$

We have chosen to normalize the mode number to the machine-averaged mode number ($<m>\sim 2.23$ on C-Mod). This makes it appropriate to compare A^* to the un-modified A, since A has the dependence on m absorbed into it and the inclusion of $<m>$ re-introduces the average of that dependence into A^*.

Figure 9 shows how this modification to the scaling improves the $<f_{rot}>$ vs $1/B_T(S/\pi)$ relationship on C-Mod. Figure 9(a) shows the isolated C-Mod data but continues to use the un-modified scaling, and colors each disruption based on whether q_{onset} was below or above 2, indicating which cases are associated with a $m=2$ or $m=3$ structure respectively. A separation in $1/B_T(S/\pi)$-space between the two cases is clear, with q_{onset} being larger for smaller values of $1/B_T(S/\pi)$. This is expected, considering that q_{onset} and the scale-factor are roughly inversely related to each other through their dependencies on S.

Figure 9(b) then shows the C-Mod data with the modified scaling given in equation (3) and shows that the trend between $\frac{<f_{rot}>}{m/<m>}$ and $1/B_T(S/\pi)$ is more linear. This increase in linearity can be seen quantitatively with the rise in the Pearson correlation coefficient by a factor of $\sim$2.6 (up to $r_{Pearson}\sim 0.34$ in linear-space and ~ 0.44 in log-space) from the un-modified to the modified version of the scaling law. A linear fit of the modified C-Mod data also gives a very similar scaling prefactor ($A^*_{CMOD}\approx 116\ [HzTm^2]$) to that found fitting the HBT-EP data ($A_{HBT}\approx 110\ [HzTm^2]$). This is significant considering that the two databases were completely isolated and live in two very different regions of parameter-space.

IV. INSENSITIVITY TO VDES AND IMPURITY EFFECTS

The characteristics of a disruption can be influenced by its cause, so it is important to investigate if the categorization of the disruption has a significant effect on the $<f_{rot}>$ scaling. This section looks at two categorizations, the vertical position and the impurity content of the plasma at the onset of the TQ. This is because of how they affect the size of the disrupting plasma and the post-TQ temperature respectively.

The vertical position of the plasma at the onset of the TQ depends on whether the plasma loses vertical stability before or after the TQ, with the disruptions of the former case being referred to as vertical displacement events (VDEs). For VDEs, the plasma will have moved significantly away from its centered position by the start of the TQ. As a result, VDE disruptions will have smaller plasmas at the onset of the TQ. This is potentially significant considering that a smaller cross-sectional area at the onset of the TQ could lead to a larger cross-section at the onset of the RHCA (an explanation of this is given in Appendix A). This could influence the HC rotation scaling because a drop in the machine's average location in $1/B_T(S/\pi)$-space would subsequently decrease its machine-

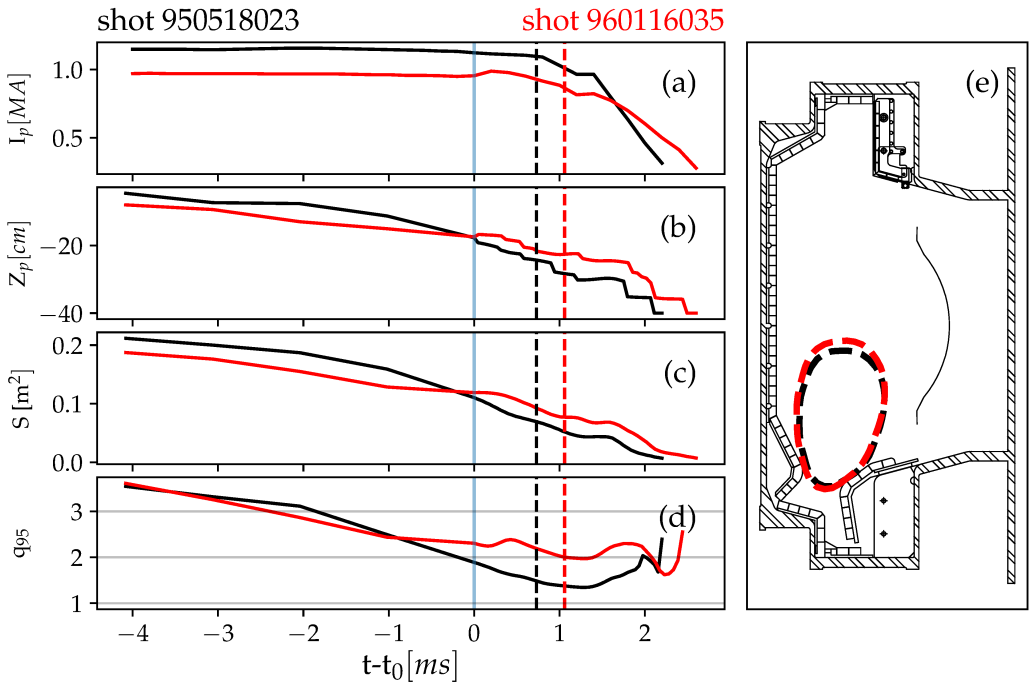

FIG. 7: Comparison of plasma parameters for two disruptions that differ primarily in I_p and q_{95}. The high-q_{95} case is in red while the low-q_{95} case is in black. Disruption curves for (a) plasma current I_p, (b) current centroid Z_p, (c) cross-sectional area S, and (d) edge safety factor q_{95}. The blue vertical line denotes the start of the CQ (the time-axis is also shifted to start here), and the dashed colored vertical lines are the RHCA onset times for both cases. (e) The LCFS of the plasma at the onset of the RHCA.

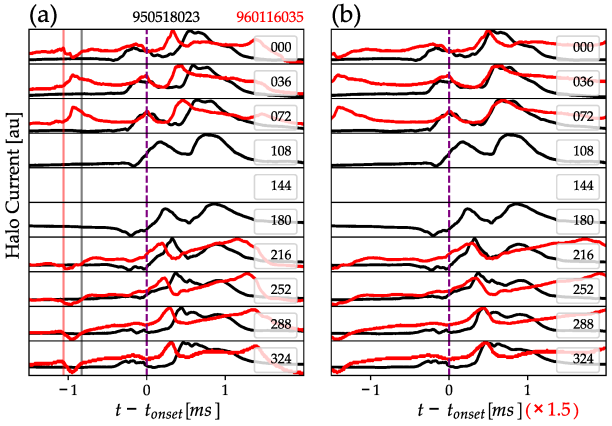

FIG. 8: Comparison of the toroidal array of HC sensors for the high- (red) and low-q_{95} (black) disruptions. The legends correspond to the toroidal position of the sensor, and the direction of increasing toroidal angle corresponds to the counter-Ip direction. The time-axis is shifted such that $t = 0$ corresponds roughly to the onset of the RHCA in each case and the colored vertical lines are the times of the current-spikes in each case. Some HC sensors where not working in either case. (a) No scaling of the time-axis. (b) The time-axis of the high-q_{95} case is scaled 1.5x.

averaged rotation frequency relative to its non-VDE disruptions.

The impurity content present in the plasma can affect the disruption in a number ways, but the most significant is its potential effect on the post-TQ temperature. One other parameters that was absorbed into the scaling coefficient (A) was a possible dependence on T_e, so significant changes in T_e due to the presence of excessive impurities could influence $<f_{rot}>$. The most significant changes to the impurity content of the plasma during disruptions tend to come from the use of impurity injection, which is often used to mitigate the effects of heat deposition and EM loads. Considering the use of impurity injections, we categorize the disruption impurity content discretely as (i) no extra impurities (un-mitigated), (ii) significant amounts of low-Z injected impurities (low-Z mitigated), and (iii) significant amounts of high-Z injected impurities (high-Z mitigated). Very few intentionally mitigated (or "killer-pellet") experiments were performed on the C-Mod database analyzed, so "mitigation-like" cases were investigated instead. In these cases, impurities were injected into the plasma for reasons other than mitigation and were not intended to disrupt the plasma. However, when too much was injected in, a disruption soon followed. We call these cases "mitigated-like", and there are many cases of this occurring ($O(30)$) for both low and high-Z impurities on C-Mod.

Figure 10(a) shows the distribution of VDE vs non-VDE

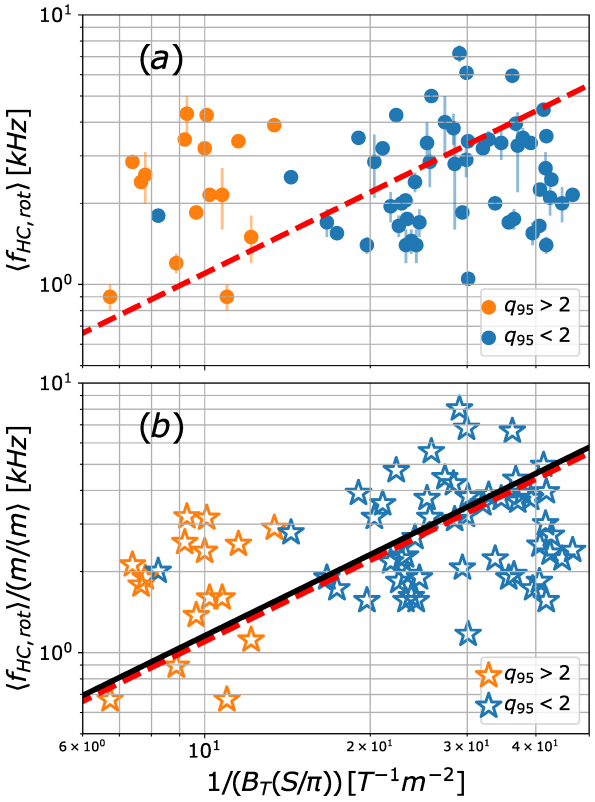

FIG. 9: C-Mod halo current rotation frequencies plotted against their scale-factors $1/B_T(S/\pi)$. Orange cases have $q_{95} > 2$ while blue cases have $q_{95} < 2$. The red dashed line is the HBT-EP scaling projected down to where this database exists. (a) Un-modified scaling. (b) Modified scaling using equation (3). The solid black line is the linear fit of the modified C-Mod frequencies.

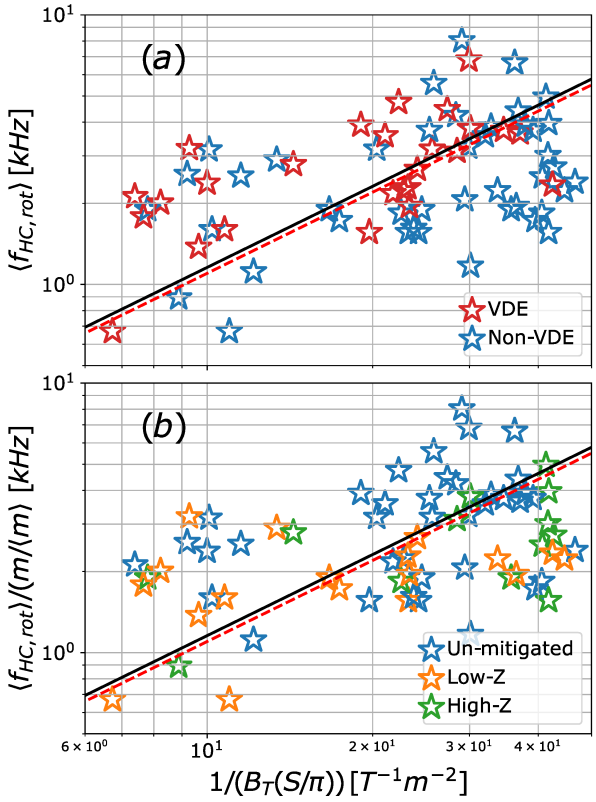

FIG. 10: Distribution of disruption categorizations in $<f_{rot}>$-$1/B_T(S/\pi)$ space for all the disruptions included in Figure 9. (a) Distribution of TQ and VDE initiated disruptions. (b) Distribution of un-mitigated, low-Z mitigated-like, and high-Z mitigated-like disruptions. These disruption categorizations do not reveal any separation in rotation or $1/B_T(S/\pi)$ behavior.

disruptions in $<f_{rot}>$-$1/B_T(S/\pi)$ space for all the disruptions included in Figure 9, and Figure 10(b) shows the distribution of un-mitigated, low-Z mitigated-like, and high-Z mitigated-like disruptions. From both, we find that neither of these differences between disruptions significantly affect the validity of the scaling. Additionally, VDE disruptions appear at similar $1/B_T(S/\pi)$ on average.

The fact that the VDE distribution is the same as that for non-VDEs implies that the size of the plasma at the onset of the RHCA does not change significantly between VDE and non-VDE disruptions. This is likely because S often drops much faster over the disruption than I_p does (between $4 \rightarrow 11$ times faster), such that the change in I_p has very little effect on the evolution of q_{95} prior to the RHCA onset and S remains similar at the onset of the RHCA, independent of it's initial value.

V. COMPARING THE TWO PARAMETERIZATIONS OF SCALING LAW

Two different parameterizations for the scaling laws provided in equations (1) and (2) have been discussed so far: a *post-TQ* and a *pre-TQ* parameterization. They differ in their specific choices of B_T and S, with the post-TQ parameterization using their values at the onset of the RHCA during the disruption and the pre-TQ parameterization using their respective machine's nominal pre-disruption values. This section compares the use of the two parameterizations to show that the more accessible one (pre-TQ) can be used in place of the more accurate one (post-TQ). A correction to the pre-TQ parameterization is also introduced based on the relationship between the two parameterizations.

The post-TQ parameterization was used in Figure 5 and in Saperstein *et al*[1] to characterize the rotation on a intra-machine basis for C-Mod and HBT-EP respectively. In contrast to this, the multi-machine analysis presented in Saperstein *et al*[1] used the pre-TQ parameterization. For the multi-machine scaling, the post-TQ parameterization would have

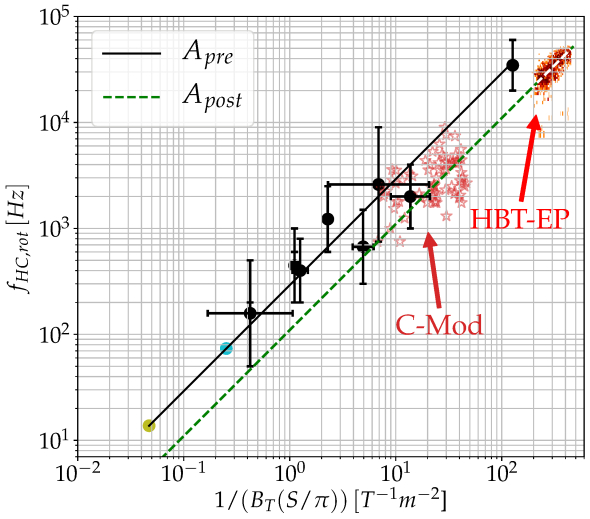

FIG. 11: Comparison of the two different scaling-law parameterizations. The black points use the pre-TQ parameterization, from various tokamaks described in Saperstein *et al*[1], while the red points use the post-TQ one. The linear fit of the pre-TQ case is shown in black, as well as the projection to SPARC (cyan) and ITER (yellow) using it. The linear fit of the HBT-EP post-TQ case is shown in the dashed green line.

been more accurate, but the parameters required to use it were not as readily available for all the tokamaks included in the scaling, so the pre-TQ parameterization was used instead.

A comparison of the two scaling parameterizations is shown in Figure 11. From this figure it can be seen that post-TQ parameterized scalings (red points, green dashed line) are similar to the pre-TQ one (black), with the scaling pre-factors for the post-TQ parameterization (A_{post}) being smaller than that of the pre-TQ parameterization (A_{pre}) by about a factor of 3. This difference is expected considering how the typical plasma-size changes between the two choices. The disrupting plasma-cross section is going to be smaller than its nominal pre-disruption counterpart, so this shifts the scaling to higher values of $1/B_T(S/\pi)$ (to the right in Figure 11) and correspondingly drops A_{post} relative to A_{pre}. The fact that the two parameterizations differ by a factor of about 3 then implies that the plasma cross-sectional area is about 3 times smaller on average during the disruption than it is pre-disruption, which is comparable to what has been observed on HBT-EP. C-Mod, however, sees a larger drop in the plasma cross-section on average, closer to about 7 times, but this is likely attributed to the fact that q_{95} at the start of the disruption is relatively large for the portion of the C-Mod database studied ($< q_{95}(C\text{-}Mod) > \sim 5.6$), implying that the plasma cross-section needs to shrink more in size to reach an unstable $q_{95} = 2$. This highlights the fact that using the pre-TQ parameterization requires a calibration factor for predicting f_{rot} that is on the order of $C_{pre} \sim \frac{<q_{95,disrupt}>_{machine}}{<q_{95,disrupt}>_{database}}$, where $< q_{95,disrupt} >_{machine}$ is the average q_{95} at the onset of the disruption for a given machine and $< q_{95,disrupt} >_{database}$ is the q_{95} at the onset of the disruption averaged over the entire multi-machine database. C_{pre} will not often exceed a factor of 2, so this will not significantly effect the validity of the scaling law given in equations (1) and (2) when making comparisons over orders of magnitude. Additionally, next generation machines will be inclined to operate at low q_{95} in order to efficiently use the magnetic fields, so a reduction in cross-sectional area during the period of interest in the disruption is expected to be closer to the ~ 3 times that's characteristic of HBT-EP.

The consistency between the pre-TQ and post-TQ parameterizations suggests that the pre-TQ values are relatively accurate at predicting a typical HC rotation frequency. This is convenient considering that pre-TQ parameters are more readily predicted when designing next generation tokamaks, like ITER and SPARC, so a parameterization of the scaling law that uses those values can be confidently used in place of the more accurate post-TQ one.

VI. DISCUSSION OF POLOIDAL ROTATION

Past reports of the rotation of the HCs during the disruption describe the rotation as toroidal[2,5,13,16]. However, this new scaling law suggests that the rotation is dominantly poloidal instead. Evidence consistent with this can be seen directly in the dependence of f_{rot} on the minor radius of the plasma (as opposed to the major radius) as well as the order of magnitude agreement between the observed rotation and the approximate electron diamagnetic drift pre-factor ($A_{\omega_e^*} \sim O(40[HzTm^2])$), but there are other factors consistent with this as well, such as the dependence of f_{rot} on q_{onset} (shown in section III) and the dependence of the direction of f_{rot} on the sign of I_p (reported in Myers *et al*[13]).

The consistency with the direction of I_p requires explanation. Myers *et al*[13] reports that the direction of observed toroidal rotation reverses with the direction of I_p (and fixed B_T), with rotation consistently being in the counter-I_p direction for all five machines included in their database. This may at first appear inconsistent with equation (1), which has no explicit dependence on I_p; however, the picture becomes clear when we consider why a poloidal rotation may be interpreted as toroidal. This conversion from a *true* poloidal rotation ($f_{poloidal}$) to an *apparent* toroidal rotation ($f^*_{toroidal}$) comes from the helicity of the rotating asymmetry, and is known as the "Barber Pole Illusion[17]." A cartoon of how the Barber Pole Illusion manifests in this context is shown in Figure 12, and the comparison between Figures 12(a) and 12(b) illustrates how reversing the direction of I_p (while keeping B_T fixed) also reverses the direction of $f^*_{toroidal}$ in the lab frame.

Considering that the Barber Pole Illusion introduces a dependence on the sign of I_p, this apparent toroidal rotation direction can also include the effect of reversing the direction of the toroidal field, since the Barber Pole Illusion (BPI) conversion is dependent on B_T as well. However, the direction of $f^*_{toroidal}$ is insensitive to the direction of B_T, because the direc-

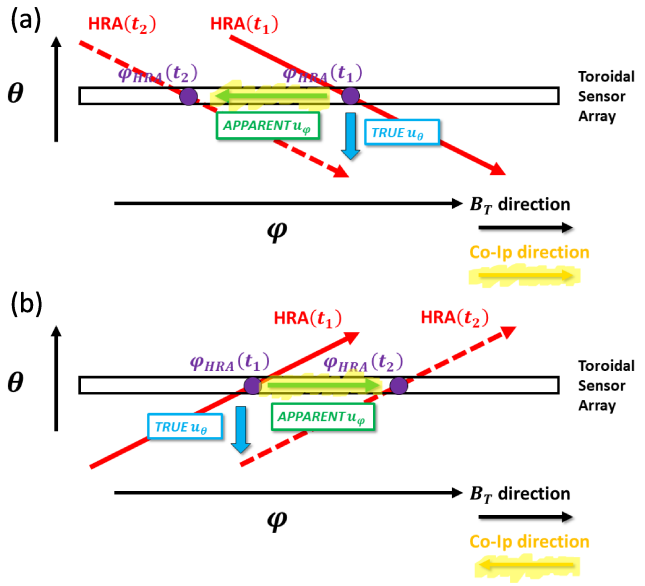

FIG. 12: Cartoons illustrating how the Barber Pole Illusion translates true poloidal rotation (blue arrow) to apparent toroidal rotation (green arrow). The red arrows denote a specific phase of a helical rotating asymmetry (HRA). The solid HRA is the initial location of that phase of the asymmetry and the dashed HRA is that same phase at a later time, translated in space as the asymmetry moves according to u_θ. The black box is some toroidal array of sensors and the purple dots denote where that array would measure that phase of the asymmetry at the given times. B_T is in the $+\hat{\phi}$, and $sign(u_\theta)$ does not change directions because it is only dependent on B_T. (a) I_p is parallel to B_T. (b) I_p is reversed to be anti-parallel to B_T.

tion of the true $f_{poloidal}$ reverses as a result of this change as well, i.e.

$$\begin{aligned} sign(f^*_{toroidal}) &= sign(f_{poloidal}) * BPI \\ &= sign(B_T) * sign(B_T)/sign(I_p) \\ &= sign(I_p) \end{aligned}$$

There have so far been no experimental reports of the effects of only reversing B_T on $f^*_{toroidal}$, but reversing both I_p and B_T on C-Mod has been shown to reverse $f^*_{toroidal}$[8], consistent with this interpretation.

The direction of apparent toroidal rotation relative to that of I_p for this conversion was also consistent with the direction of poloidal rotation that was observed on HBT-EP. HBT-EP has both fast-camera imaging and magnetic measurements showing that the poloidal rotation is in the electron-diamagnetic drift direction, which is consistent with the Barber Pole Illusion converting it to an apparent counter-I_p toroidal rotation.

VII. CONCLUSION

This paper validates the use of the scaling law given in equation (1) on Alcator C-Mod and highlights some of the additional effects that may impact the rotation physics of asymmetric halo currents. We found that the average rotation frequency observed on C-Mod agreed well with that predicted by the HBT-EP-calibrated scaling, and that if the poloidal structure of the RHCAs (measured via q_{onset}) are taken into account, then the isolated C-Mod data reproduced the same linear trend between $<f_{rot}>$ and $1/B_T(S/\pi)$ that was observed on HBT-EP, down to a scaling pre-factor (A) that agreed to within $\sim 5\%$. This agreement is remarkable considering the large separation in parameter-space between the two machines, and lends credibility to the use of a low field, high aspect ratio device such as HBT-EP as an anchor in validating the scaling law at high values of $1/B_T(S/\pi)$. Additionally, this agreement supports the use of the updated version of the scaling law given in equation (2), which accounts for plasmas with non-circular cross-sections.

Important additional effects highlighted by the analysis of C-Mod include (i) the dependence on q_{onset} (through its relationship to m) and (ii) the stagnation of the evolution of the rotation. The stagnation was noted in a previous multi-machine analysis[13], but the q_{onset} (and m) dependence is reported here for the first time. This m-dependence modifies the scaling law to that given in equation (3), which should be used when the m-number is known. The stagnation of the evolution of the rotation refers to f_{rot} not continuously increasing as the plasma shrinks following the onset of the RHCA, as the scaling law would predict and has been seen to occur on HBT-EP.

Some effects were less significant. These include the effects of VDEs and impurity injection, neither of which significantly affect the distribution of rotation frequencies in $1/B_T(S/\pi)$-space. While VDEs were not expected to affect the validity of the scaling, there was a potential for them to shift the distribution in $1/B_T(S/\pi)$-space, decreasing the machine averaged rotation frequency. However, this effect was not observed. The introduction of impurities also did not appear to affect the distribution, but the analysis of intentionally mitigated disruptions should still be done to verify this.

The use of the pre-TQ parameterization of multi-machine scaling was also found to be valid through comparisons to the more accurate post-TQ parameterizations of HBT-EP and C-Mod. This is useful because pre-TQ parameters are more readily accessible, simplifying the projections for next generation machines, which can be made using equation (2) with a scaling pre-factor of $A = 292$ $[HzTm^2]$. The most significant disagreement appears to come from differences in q_{95} prior to the disruption, but this likely will not introduce errors larger than a factor of 2 provided q_{95} does not vary significantly from tokamak-to-tokamak.

Lastly, several observations are consistent with the dominance of poloidal rotation during the disruption, which was suggested by the poloidal drift motivation of the scaling law. These observations included the dependence of f_{rot} on (i) the minor radius (instead of the major radius), (ii) q_{onset}, and (iii) the direction of I_p. The recognition of the possible dominance

of poloidal rotation is not only useful for explaining the observed rotation, but it may also prove useful for simulating disruptions in the future.

ACKNOWLEDGMENTS

This work was supported by U.S. Department of Energy, Office of Science, Office of Fusion Energy Science, Grant DE-FG02-86ER53222. We would also like to thank the rest of the HBT-EP team, as well as Chris Hansen, Clayton Myers, and Ryan Sweeney for their useful discussions.

Appendix A: VDE plasma size

This appendix section clarifies how a smaller plasma cross-section at the onset of the disruption may lead to a larger plasma cross-section at the onset of the RHCA. This characteristic follows from the constraint that the RHCA will nominally become unstable at some specific value of q_{95}, which is dependent on both I_p and S. The relationship is approximately

$$q_{95} \propto \frac{S}{I_p} \tag{A1}$$

which suggests I_p and S have inverse effects on q_{95}. Both S and I_p are monotonically decreasing functions over the course of the CQ, so whether or not q_{95} increases or decreases depends on which one is changing faster. In order for q_{95} to drop and eventually reach an unstable value (q_u), S needs to drop faster than I_p. This is often what's observed for many disruptions, including the ones discussed in this paper.

In the case where S drops significantly faster than I_p, then the evolution of q_{95} is dominantly dependent on the change in S. q_{95} will then approach an unstable value before I_p can change significantly. As a result, q_{95} would always reach the unstable value at the same value of S (if I_p starts at the same value), because its evolution doesn't significantly depend on any other variables.

Now instead, consider the case where the rate at which I_p drops is smaller, but comparable, to the rate for S. In this case, q_{95} will eventually reach that same unstable value, but it will take a longer amount of time because the drop in I_p has the inverse effect of the drop in S. This longer decay time, in conjunction with $d_t I_p$ being comparable to $d_t S$, then implies that I_p will have dropped some significant amount by the time q_{95} reaches the unstable value (at time t_u following the TQ). Exactly how much I_p changes over the time t_u will then influence what S at t_u ($S(t_u) = S_u$) will be. We can compare what S needs to be to reach q_u for the cases where S at the onset of the disruption is either larger (S_{0+}) or smaller (S_{0-}). An example for this case is illustrated in Figure 13, where S_- starts off only $3/4$ the size of S_+, but both cases have the same I_p-evolution and S exponential-decay rate (which is larger than the I_p linear-decay rate by a factor of 3). Figure 13(c) shows that the smaller case (the VDE) will reach the unstable q-value (in this case $q_u = 2$) earlier in time than the larger case (non-VDE). Now because both cases have the same I_p-evolution, Figure 13(a) shows that the VDE case will have a larger plasma current when passing q_u ($I_{p,-u}$) than the non-VDE case ($I_{p,+u}$), resulting in a larger plasma size at that time ($S_{-u} > S_{+u}$) by about a factor of $1.3x$. The implications of this last statement can also be expressed quantitatively using the equality below

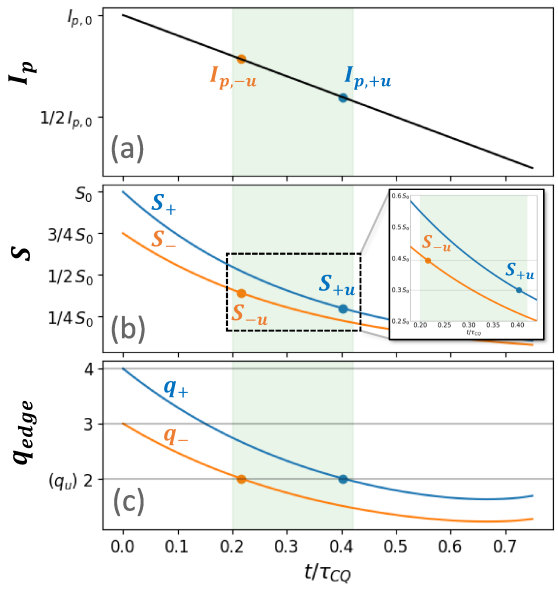

FIG. 13: Comparison of two example disruptions showing that a plasma that starts off smaller may actually have a larger cross-section when it crosses an unstable value of q (q_u). The blue curves/points correspond the larger plasma and the orange curves/points correspond to the smaller one. (a) The evolution of I_p, which is modeled as a linear decay. (b) The evolution of the plasma cross-sectional area, which is modeled as an exponential decay, with a decay rate faster than that for I_p by a factor of $3x$. The inset zooms in on the green region. (c) The evolution of q_{95}, resulting from the given I_p and S-curves assuming $q_{95} \propto S/I_p$.

$$q_u \sim \frac{S_u}{I_{p,u}} = \frac{S_{+u}}{I_{p,+u}} = \frac{S_{-u}}{I_{p,-u}} \tag{A2}$$

which uses the assertion that q_u must be the same for both cases to constrain the relationship between $S_{+u}/I_{p,+u}$ and $S_{-u}/I_{p,-u}$. Since $I_{p,-u} > I_{p,+u}$, equation (A2) enforces $S_{-u} > S_{+u}$, suggesting that the plasma at q_u will be larger if the it started off smaller at the onset of the disruption.

[1] A.R. Saperstein, J.P. Levesque, M.E. Mauel and G.A. Navratil, "Halo current rotation scaling in post-disruption plasmas", 2022 Nucl. Fusion **62** 026044; https://doi.org/10.1088/1741-4326/ac4186

[2] H. Strauss, L. Sugiyama, R. Paccagnella, J. Breslau and S. Jardin, "Tokamak toroidal rotation caused by AVDEs and ELMs", 2014 Nucl. Fusion **54** 043017; doi:10.1088/0029-5515/54/4/043017

[3] Janardhan Manickama, Allen Boozer, and Stefan Gerhardt, "Kink modes and surface currents associated with vertical displacement events", 2012 Phys. Plasmas **19** 082103; https://doi.org/10.1063/1.4740507

[4]Leonid E. Zakharov, Sergei A. Galkin, Sergei N. Gerasimov, and JET-EFDA contributors, "Understanding disruptions in tokamaks", 2012 Phys. Plasmas **19** 055703; http://dx.doi.org/10.1063/1.4705694

[5]A.H Boozer, "Rotation of tokamak halo currents", 2012 Phys. Plasmas **19** 052508; https://doi.org/10.1063/1.4717721

[6]A.H. Boozer, "Characteristic time for halo current growth and rotation", 2015 Phys. Plasmas **22**, 102511; https://doi.org/10.1063/1.4933363

[7]T.E. Evans, C,J. Lasnier, D.N. Hill, A.W. Leonard, M.E. Fenstermacher, T.W. Pertie, and M.J. Sschaff, "Measurements of non-axisymmetric effects in the DIII-D divertor", 1995 J. Nucl. Mater. **220–222** 235; https://doi.org/10.1016/0022-3115(94)00419-6

[8]R.S. Granetz, I.H. Hutchinson, J. Sorci, J.H. Irby, B. LaBombard, D. Gwinn, "DISRUPTIONS AND HALO CURRENTS IN ALCATOR C-MOD", 1996 Nucl. Fusion **36** 545; doi 10.1088/0029-5515/36/5/I02

[9]H. Takahashi, E.D. Fredrickson, M.J. Schaffer, M.E. Austin, T.E. Evans, L.L. Lao and J.G. Watkins, "Observation of SOL current correlated with MHD activity in NBI heated DIII-D tokamak discharges", 2004 Nucl. Fusion **44** 1075; doi:10.1088/0029-5515/44/10/003

[10]S.P. Gerhardt, "Dynamics of the disruption halo current toroidal asymmetry in NSTX", 2013 Nucl. Fusion **53** 023005; doi:10.1088/0029-5515/53/2/023005

[11]S.N. Gerasimov, T.C. Hender, J. Morris, V. Riccardo, L.E. Zakharov and JET EFDA Contributors, "Plasma current asymmetries during disruptions in JET", 2014 Nucl. Fusion **54** 073009; doi:10.1088/0029-5515/54/7/073009

[12]J.P. Levesque, J.W. Brooks, M.C. Abler, J. Bialek, P.J. Byrne, C.J. Hansen, P.E. Hughes, M.E. Mauel, G.A. Navratil and D.J. Rhodes, "Measurement of scrape-off-layer current dynamics during MHD activity and disruptions in HBT-EP", 2017 Nucl. Fusion **57** 086035; https://doi.org/10.1088/1741-4326/aa75ea

[13]C.E. Myers, N.W. Eidietis, S.N. Gerasimov, S.P. Gerhardt, R.S. Granetz, T.C. Hender, G. Pautasso and JET Contributors, "A multi-machine scaling of halo current rotation", 2018 Nucl. Fusion **58** 016050; https://doi.org/10.1088/1741-4326/aa958b

[14]E. Marmar 2018 "Alcator C-Mod, Final Technical Report"; https://doi.org/10.2172/1457696

[15]F. J. Artola, C. R. Sovinec, S. C. Jardin, M. Hoelzl, I. Krebs, and C. Clauser, "3D simulations of vertical displacement events in tokamaks: A benchmark of M3D-C1, NIMROD, and JOREK", 2021 Phys. Plasmas **28**, 052511; https://doi.org/10.1063/5.0037115

[16]H. Strauss, "Asymmetric wall force and toroidal rotation in tokamak disruptions", 2015 Phys. Plasmas **22**, 082509; https://doi.org/10.1063/1.4928582

[17]L.E. Dodd, "The Stroboscopic Effect and the Barber-Pole Illusion", 1954 American Journal of Physics **22**, 394; https://doi.org/10.1119/1.1933755